

## Mixing of Subtropical, Central, and Intermediate Waters Driven by Shifting and Pulsing of the Agulhas Current

KATHRYN L. GUNN,<sup>a</sup> LISA M. BEAL,<sup>a</sup> SHANE ELIPOT,<sup>a</sup> K. MCMONIGAL,<sup>a</sup> AND ADAM HOUK<sup>a</sup>

<sup>a</sup> *Rosenstiel School of Marine and Atmospheric Science, University of Miami, Miami, Florida*

(Manuscript received 30 April 2020, in final form 30 September 2020)

**ABSTRACT:** The Agulhas Current, like all western boundary currents, transports salt from the subtropics toward the poles and, on average, acts as a barrier to exchange between the open ocean and continental seas. Uniquely, the Agulhas jet also feeds a leakage of relatively salty waters from the Indian Ocean into the Atlantic Ocean. Despite its significance, the signals and drivers of water mass variability within the Agulhas Current are not well known. To bridge this gap, we use 26 months of moored observations to determine how and why salinity—a water mass tracer—varies across the Agulhas Current. We find that salinity variability is driven by both shifting (i.e., changes in location) and pulsing (i.e., changes in strength) of the current. Shifting of the current causes heave and diapycnal mixing of subtropical, central, and intermediate waters. Diapycnal mixing between central and intermediate waters explains most of the variability, creating salinity anomalies between  $-0.4$  and  $+0.1$  psu. Pulsing of the current drives heave and, to a lesser extent, along-isopycnal mixing within the halocline. This cross-stream mixing results in salinity anomalies of up to  $0.3$  psu. The mean and standard deviation of Agulhas Current volume and salt transports are  $-76$  and  $22$  Sv ( $1$  Sv  $\equiv 10^6$  m<sup>3</sup> s<sup>-1</sup>) and  $-2650$  and  $770$  Sv psu. Transport-weighted salinity has a standard deviation of  $0.05$  psu. We estimate that  $O(10^{13})$  kg yr<sup>-1</sup> of the salt transported southwestward leaks into the fresher Atlantic Ocean. On the basis of our observations, the variability of the Agulhas Current could alter this salt leakage by an order of magnitude.

**KEYWORDS:** Indian Ocean; Mixing; Salinity; In situ oceanic observations; Empirical orthogonal functions; Oceanic variability


### 1. Introduction

The Agulhas Current hugs the South African coastline and, on average, acts as a barrier between the shallow shelf seas and open ocean (Bower et al. 1985; Beal et al. 2006). It is expected that, like other western boundary currents, variability in the Agulhas Current will alter the distribution and properties of water masses across the shelf and within the current itself. However, a paucity of observational data spanning the current has hampered efforts to determine how and why water masses vary. Here, we address this gap in our knowledge by analyzing the spatiotemporal variability of salinity—a conservative tracer of water masses—across the current.

Variability of water masses in the Agulhas Current has been previously inferred using infrequent hydrographic transects. Four hydrographic transects, collected over a period of three years, revealed changes in temperature and salinity of  $1^{\circ}\text{C}$  and  $0.25$  psu at shallow and intermediate depths (Fig. 4 of Leber and Beal 2015). Of these transects, one captured the Agulhas Current during a meander, whereby the jet shifts laterally offshore by approximately  $100$  km. Meandering drives isopycnal uplift of  $O(100)$  m which cools and freshens water above the thermocline and on the shelf (e.g., Bryden et al. 2005; Goschen et al. 2012, 2015). As the meander propagates southwestwards, its trailing edge induces downwelling of similar magnitudes (Campos et al. 2000; Malan et al. 2018).

Hence, this variability, caused by heave of water masses, is reversible. In their study, Leber and Beal (2015) also found that the meander induced irreversible variability in the form of diapycnal mixing. With the available data, it was not possible to determine the generality of these processes or the proportions of reversible (i.e., heave) and irreversible (i.e., mixing) variability. Since then, hydrographic measurements across the Agulhas Current have remained temporally discrete and infrequent. Thus, the subsurface drivers of water mass variability, and their effects, have yet to be diagnosed.

As well as impacting water mass properties locally, the Agulhas Current leaks water into the Atlantic Ocean. At the retroflection, a proportion of salty Indian Ocean water enters the fresher southeast Atlantic Ocean. Several modeling and paleoceanography studies suggest that Agulhas leakage may affect the stability and strength of Atlantic overturning circulation (e.g., Weijer et al. 1999; Simon et al. 2013; Biastoch et al. 2008; Weijer et al. 2019). Marsh et al. (2007) found that collapse of this circulation is 5 times more likely if Agulhas leakage is the dominant process in maintaining high Atlantic salinities. A portion of this leakage is facilitated by saline rings of Agulhas water that transport salt to the South Atlantic at a rate of  $O(10^8\text{--}10^{13})$  kg yr<sup>-1</sup> and cause salinity anomalies of up to  $0.2$  psu in the South Atlantic thermocline (van Ballegooyen et al. 1994; McDonagh et al. 1999; Gordon 1985). However, recent modeling studies suggest that over 50% of leakage occurs

 Denotes content that is immediately available upon publication as open access.

Corresponding author: Kathryn Gunn, kathy.gunn@csiro.au

*Publisher's Note:* This article was revised on 10 March 2021 to correct a production error that appeared in the corresponding author email address and include the addition of the last sentence in the Acknowledgments.

DOI: 10.1175/JPO-D-20-0093.1

© 2020 American Meteorological Society. For information regarding reuse of this content and general copyright information, consult the AMS Copyright Policy ([www.ametsoc.org/PUBSReuseLicenses](http://www.ametsoc.org/PUBSReuseLicenses)).

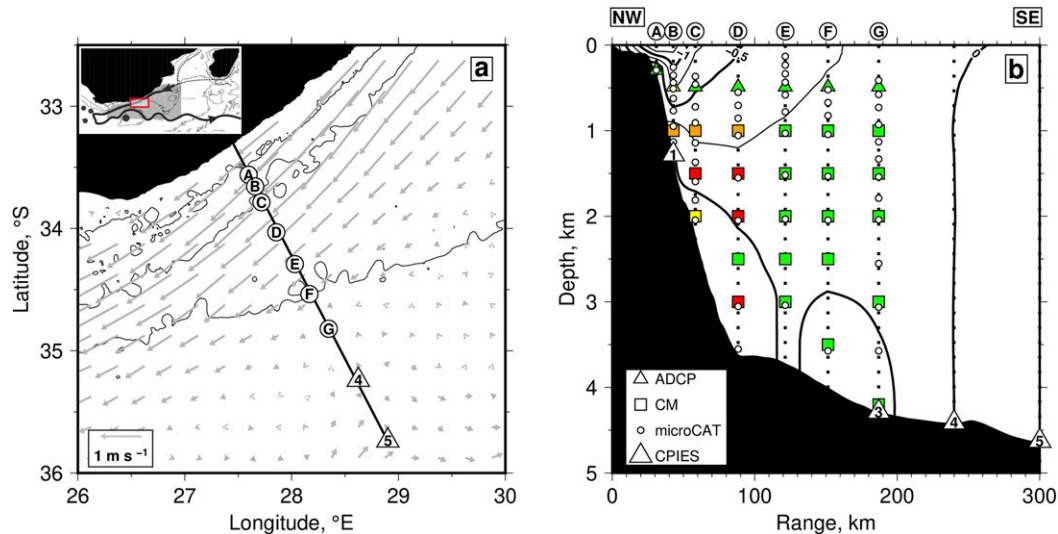


FIG. 1. Agulhas Current and ASCA at 34°S: (a) Regional and local context of ASCA experiment. Black shading = South Africa; thick black line = ASCA extent; labeled white circles = loci of moorings A–G; white triangles = loci of CRIES 4 and 5 (collocated CRIES 1 and 3 are at moorings B and G, respectively); thin black lines = 300- (i.e., ~continental shelf edge), 2000-, and 4000-m bathymetric contours; gray arrows = annual drifter-derived near-surface currents. Inset = Indian Ocean basin between 15° and 45°S and between 15° and 50°E; red-outlined box = region shown in (a); black lines and circles = schematic of Agulhas Current, its retroflection, and its return current plus leaked Agulhas rings; dark-gray circles = regional hydrographic data used to construct GEM and local  $T$ - $S$  relationships. (b) Vertical cross section showing array design. Black shading = seafloor; colored triangles and squares = time-mean pressure levels of upward-looking ADCPs and CMs, respectively, colored by recovery percentage (i.e., green = 100%; yellow  $\geq$  70%; orange  $\leq$  50%; red  $\leq$  40%); white circles = time-mean pressure levels of moored CTD instruments (microCAT); white triangles = CRIES 1, 3, 4, and 5; dotted lines = vertical extent of moorings; solid black lines = contours of ASCA time-mean along-stream velocity every  $0.25 \text{ m s}^{-1}$ , where negative values indicate southwestward flow out of the page.

outside of these rings (Biaostoch et al. 2008; Rouault et al. 2009). Furthermore, the hitherto discrete nature of hydrographic data has hampered our understanding of the magnitude of variability of leakage salt fluxes (Reason et al. 2003). Thus, an updated observational estimate of Indian–Atlantic salt flux, and its variability, is needed.

Here, we address these gaps in our knowledge using the first time series of temperature and salinity collected across the Agulhas Current. Between 2016 and 2018, temperature, salinity, and velocity time series were collected as part of the Agulhas System Climate Array (ASCA) experiment. ASCA is a continuation and expansion of the Agulhas Current Time-series (ACT) experiment which recorded velocity time series between 2010 and 2013 (Beal et al. 2015; Elipot and Beal 2015; Beal and Elipot 2016). These two experiments are collocated at 34°S. McMonigal et al. (2020) use temperature and velocity records collected during ASCA to examine the impact of meandering, broadening, and seasonality on temperature variability. Here, we use the salinity and velocity records to analyze the spatiotemporal variability of salinity—a water mass tracer—across the Agulhas Current. First, we construct and analyze salinity and velocity sections every 20 h over a 26-month period. Second, we present the leading modes of water mass variability in both depth and density space, diagnose signatures of isopycnal heave and mixing, and relate these to changes in the position and strength of the current. Third, we combine our measurements with a new Lagrangian estimate of Agulhas leakage to estimate Indian–Atlantic salt flux.

## 2. Data and methods

### a. Array design and instrumentation

Seven tall moorings, A–G, were outfitted with seven acoustic Doppler current profilers (ADCPs), 23 current meters (CMs), and 56 moored conductivity–temperature–depth instruments (microCAT; Fig. 1). Moorings A–G are augmented by four Current and Pressure Recording Inverted Echo Sounders (CRIESs) and extend the mooring array 300 km from the coast (Fig. 1). CRIESs 1 and 3 are collocated at Mooring B and G, respectively (Fig. 1b). CRIESs 3, 4, and 5 provide estimates of geostrophic velocity beyond the tall moorings. In total, 90 instruments were deployed at nine sites across the Agulhas Current (mooring A, mooring B/CRIES 1, moorings C–F, mooring G/CRIES 3, CRIES 4, and CRIES 5). The average horizontal and vertical spacing between instruments is 30 and 0.3 km, respectively (Fig. 1b). The array follows a satellite altimetry ground track and is oriented 15° from normal to the main jet of the Agulhas Current.

### b. Data

Point measurements of pressure, temperature  $T$ , and conductivity were recorded every 20 min by 56 microCATs. Conductivity measurements were converted into salinity  $S$  following the methods of Kanzow et al. (2006). All records were quality controlled to remove spikes and spurious data points. The measurements recorded by microCATs yielded

water mass properties up to 187 km from the coastline (Fig. 1b, white circles).

CPIESs were used to extend the array to 300-km range (Fig. 1b, white triangles). CPIESs are bottom-deployed instruments that measure acoustic round-trip travel time  $\tau$ , which is directly related to the integrated properties of the water column (Watts and Rossby 1977). When  $\tau$  is combined with measured near-bottom pressures and velocities as well as a lookup table of hydrographic data, full-depth vertical profiles of  $T$  and  $S$  can be derived [for more details, see Donohue et al. (2010) and Beal et al. (2015)]. This method, known as the gravest empirical mode (GEM) method, makes no assumptions about the vertical hydrographic structure and instead fits data empirically (Meinen and Watts 2000). To build the GEM we used all hydrographic profiles extending to depths greater than 1900 dbar within the region 28°–40°S and 21°–37°E from the World Ocean and Argo databases (Fig. 1a, inset; <http://www.argodatamgt.org> and <https://www.nodc.noaa.gov>; Boyer et al. 2018). Using the lookup table, the CPIESs yielded continuous vertical profiles of  $T$  and  $S$  every 20 min. CPIES pairs 3–4 and 4–5 were used to estimate geostrophic velocity shear, which was referenced to measure near-bottom velocities at CPIESs 3, 4, and 5 to provide absolute along-stream velocities (Fig. 1b, 187–300-km range). In this way, the along-stream velocity field was extended to 300-km range.

CMs that recorded every 20 min yield direct along-stream ( $v$ ) and cross-stream velocity measurements at moorings A–G (Fig. 1b, colored squares). Direct velocity measurements between the sea surface and 500 m are provided by hourly ensembles from upward-looking ADCPs (Fig. 1b, colored triangles). Typically, the shallowest ADCP bin was between 60 and 70 m. However, blow-down in regions of strong flow often decreased the effective shallowest depth to 200–250 m. Eight CMs suffered from instrument failure yielding incomplete records. Linear regression models were employed to reconstruct shortened records to 26-month time series. Since multiple neighboring CMs failed, multiple dependencies arose. For example, the deepest CM at mooring D was reconstructed using the CM above and to the southeast (Fig. 1b). The uncertainty associated with the missing records and multiple linear regression is estimated in the appendix, section b.

The ability of the instrument configuration to resolve the observed flows can be assessed by evaluating the vertical and horizontal decorrelation length scales of the  $T$ ,  $S$ , and  $v$  fields and comparing those to the instrument spacing. We followed the method of Beal et al. (2015), whereby covariance functions are fit to the correlations between pairs of 40-h low-passed  $T$ ,  $S$ , and  $v$  records as a function of their separation distance [for more details, see Eqs. (A1) and (A2) of Beal et al. 2015]. The minimum separation distance for which the correlation becomes zero gives an indication of the decorrelation length scale (i.e., the spatial limit to which ocean properties coherently vary). For  $T$ ,  $S$ , and  $v$ , the horizontal and vertical scales of the flow are approximately 60 km, about 2 times the horizontal average separation of the mooring sites, and 1500 m, about 5 times the average vertical separation of the sites. Beyond the typical location of the jet (i.e., offshore of 190 km),

CPIESs are spaced 50–60 km apart horizontally. Therefore, we are confident that the instrument configuration is able to resolve  $T$ ,  $S$ , and  $v$  fields across the Agulhas Current.

### c. Construction of gridded fields

We applied a low-pass filter to each instrument's time series with a 40-h cutoff to remove inertial, diurnal and semidiurnal variability. The measurements were subsampled giving  $T$ ,  $S$ , and  $v$  at 20-h intervals and at discrete pressure levels corresponding to the instrument depths (Fig. 2a, black circles). However, spatially continuous profiles were desirable to investigate water mass distribution and variability.

#### 1) SALINITY

Since the in situ microCAT measurements do not reach the sea surface (e.g., Fig. 2b, red circles), satellite data were used to provide measurements of sea surface salinity. Satellite-derived salinity products have neither a spatial nor temporal resolution that is comparable with measurements from ASCA (e.g., ESA's Soil Moisture Ocean Salinity; Kerr et al. 2001). Therefore, we used sea surface temperature measurements from the Group for High Resolution Sea Surface Temperature alongside a local  $T$ – $S$  relationship to recover surface salinities (GHRSSST; Martin et al. 2012). Temperature–salinity relationships were derived for each mooring using the same CTD and Argo casts that are used for the GEM, then windowed using a box of 50 km<sup>2</sup> around each mooring (Fig. 2a).

Temperature and salinity measurements from the surface to 20 dbar were then used to derive a linear  $T$ – $S$  relationship (Fig. 2b, black line). In this way, seven local  $T$ – $S$  relationships were estimated and used to convert SST into sea surface salinity at daily resolution for each mooring (time series are interpolated to 20-h intervals to match the time steps of ASCA). The cross-stream near-surface gradient of salinity is well recovered and consistent with earlier publications (i.e., salinity increases with offshore distance; Beal et al. 2006; Russo et al. 2019).

In the CPIES region, full-depth profiles of  $T$  and  $S$  were generated using  $\tau$  and regional data from the GEM. However, since these regional data are deseasoned there is little variation in upper water column structure in the CPIES region. Therefore, we reconstructed seasonality in the upper ocean using the satellite data. We assumed that calculated sea surface salinities are correct at 0-m depth and that CPIES measurements are accurate between 200-m depth and the seafloor. Then  $S$  was interpolated from the sea surface to 200-m depth.

Using daily sea surface measurements, we were able to recover a portion of seasonality in the upper 200 m. When the gridded product is compared with collocated CTD sections, the surface root-mean-square (rms) sampling error is 0.1 psu (see the appendix, section a, for further details and Fig. A1a, yellow line). Using piecewise cubic Hermite interpolation upward from the shallowest microCAT (i.e., not using daily sea surface measurements) increases the surface error by 40%. It was not possible to recover the seasonality using an empirical model of local  $T$  and  $S$  (as is the case in Watts et al. 2001), due to the low temporal sampling of in situ data in this region. Thus, we found that using satellite data recovers a portion of the

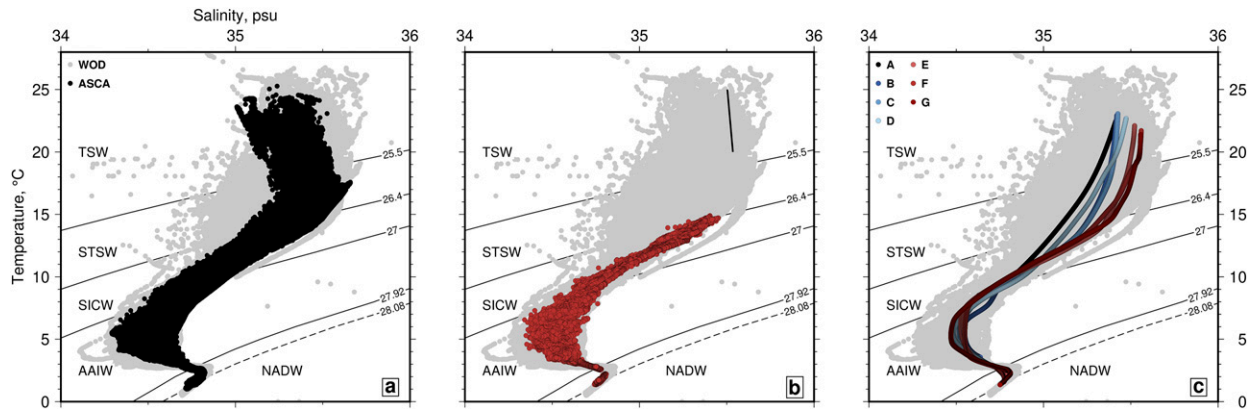


FIG. 2. Temperature–salinity diagrams showing  $T$ – $S$ – $\gamma$  properties and construction of gridded fields: (a) Gray points = regional  $T$ – $S$  measurements ( $28^{\circ}$ – $40^{\circ}$ S,  $21^{\circ}$ – $37^{\circ}$ E of World Ocean Database as shown in inset of Fig. 1a); black points =  $T$ – $S$  data recorded by ASCA; solid black lines = neutral density  $\gamma$  surfaces of labeled water masses (see section 2c); dashed black line = Lower NADW, which is not observed by the ASCA experiment. (b) Red points =  $T$ – $S$  recorded at mooring G (note: the shallowest microCAT lies at  $\sim 500$ -m depth); thin black line = local, near-surface  $T$ – $S$  relationship calculated for this site. The other symbols are as in (a). (c) Time-mean vertical profiles constructed for moorings A–G. Colored circles = time-mean  $T$ – $S$  structure at each mooring colored by distance from coast (see the key). The other symbols are as in (a).

seasonal cycle (such that 15% of temperature variability in the region is explained by seasonal variations; McMonigal et al. 2020), while also minimizing the surface rms error.

After the near-surface salinities were reconstructed, subsurface measurements were spatially interpolated. In contrast to interpolation of temperature, it is not possible to use climatology-derived salinity gradients here, since the salinity gradient does not monotonically change within the vertical spacing of microCATs (e.g., Johns et al. 2005; McCarthy et al. 2015). Instead, salinity was estimated vertically at each mooring using piecewise cubic Hermite interpolating polynomials (using the measured rather than deployed pressure). Below the deepest microCAT at each mooring, salinity was extrapolated as a constant. Linear interpolation was used in the horizontal between mooring A and CRIES 5. Inshore of mooring A, salinity was extrapolated assuming a constant horizontal gradient calculated between moorings A and B. In this way, a salinity section was created for each time step (i.e., every 20 h between April 2016 and June 2018) that has horizontal and vertical spacing of 500 m and 20 dbar, respectively.

Time-mean  $T$ – $S$  profiles recover the cross-stream gradients of salinity well (Fig. 2c). Cross-stream salinity gradients, of  $O(10^{-3})$  psu  $\text{km}^{-1}$ , are greatest within Tropical and Subtropical Surface Waters (TSW and STSW), as well as South Indian Central Water (SICW), and are consistent with horizontal gradients found at  $36^{\circ}$ S (Fig. 2c; Beal et al. 2006). The shallow local maximum of STSW is not well resolved because of a lack of measurements in the upper water column, which led to a fresh salinity bias in the upper water column of 0.03 psu (e.g., Fig. 2b). This bias is corrected for (see the appendix for more details). For the same reason, salinity uncertainties are surface intensified. At the sea surface, the total uncertainty reaches 0.15 psu (Fig. A1, black line). At 500- and 2000-m depth, the uncertainty reduces to 0.08 psu and  $\leq 0.01$  psu, respectively. The depth-averaged salinity error is 0.05 psu. Overall, the long-

wavelength vertical structure is well resolved in the upper 500 m (primarily TSW and STSW). The short- and long-wavelength vertical  $T$ – $S$  structure for all other water masses is recovered well (Fig. 2c). Since isopycnals slope sharply in this region we use contours of time-mean neutral density  $\gamma$ , which are calculated using the Thermodynamic Equation of SeaWater 2010 (TEOS-10) lookup table, to constrain water masses (Jackett and McDougall 1997; Beal et al. 2006).

## 2) VELOCITY

Velocity time series for one ADCP and seven CMs that did not record for the entire deployment were extended using sequential multiple linear regression models based on nearby instrumental records. The full-length velocity records were low-pass filtered with a 40-h cutoff to remove inertial, diurnal, and semidiurnal variability then subsampled every 20 h. The velocity records were interpolated to a regularly spaced grid following the method described in Beal et al. (2015). The final velocity section was sampled at 500-m and 20-dbar spatial intervals.

### d. Transport time series

Volume transport is given by

$$\iint v dx dz. \quad (1)$$

We followed Beal et al. (2015) to define limits of integration. First, a “box” transport  $T_{vb}$  was calculated between the coastline and the mean width of the jet demarcated by the outcropping of the zero isotach (219 km on average). Here,  $T_{vb}$  provides a measure of volume transport that is consistent with earlier estimates (e.g., Bryden et al. 2005). Second, transport was calculated using limits that change with time,  $T_v$ . These boundaries were defined using the strength and cross-sectional area of the Agulhas jet at each time step [for further details, see

Beal et al. (2015)]. We refer to  $T_v$  as the “jet” definition;  $T_v$  is able to account for the effect of meanders because it is not constrained by fixed integration limits. However, since northeastward flows are excluded,  $T_v$  may be biased high (positively) by local recirculations.

Salt transport  $T_s$  is given by

$$\iint Sv \, dx \, dz. \quad (2)$$

The units used here are Sv psu ( $1 \text{ Sv} = 10^6 \text{ m}^3 \text{ s}^{-1}$ ). At each time step,  $T_s$  was calculated using the jet-defined limits of integration. We do not calculate freshwater transport here since it requires mass conservation to be meaningful (e.g., Schauer and Losch 2019) and this balance is not possible with data solely from ASCA.

### e. Empirical orthogonal function analysis

The variability of the salinity field across the Agulhas Current was investigated using empirical orthogonal function (EOF) analysis. This method decomposes the time–space matrix of salinity measurements into the sum of space-dependent mode patterns multiplied by time-dependent amplitudes, also known as principal components, for each mode. Variability that emerges from EOF analysis conducted in depth space should be considered a measure of the total salinity variance, which can be either reversible or irreversible. Reversible variability is caused by spatial displacements such as heave. Irreversible variability is caused by mixing. To isolate irreversible variability, the salinity field was recast into neutral density space and empirical orthogonal function analyses were recalculated (DEOF). Thus, if no anomaly is present in density space, variability is purely reversible.

The drivers of salinity variability were investigated by comparing each principal component to the time-varying anomalous depths and thicknesses of each water mass within the section. Using the time-varying neutral density field, and  $\gamma$ -based water mass definitions of Beal et al. (2006), the depth and thickness of each water mass was estimated at each mooring. Depth and thickness anomalies were calculated by removing their time mean. Anomaly time series were compared with each mode, and their correlation was calculated. Correlations between the time series are expressed as Pearson’s correlation  $r$ . Here,  $r > 0.2$  are significant at the 95% threshold (Beal et al. 2015). It is important to note that the calculated patterns do not change with the removal of random time steps or portions of the water column (e.g., upper 500 m), indicating that the observed variance is robust. Thus, we are able to determine the most likely physical mechanisms driving the salinity—and therefore water mass—variability associated with each mode.

## 3. Results

### a. Time-mean structure

We find that the time-mean velocity structure of the Agulhas Current during ASCA is similar to that for the ACT experiment. The Eulerian mean Agulhas Current, between April 2016 and

June 2018, is 260 km wide with peak surface speeds of  $-1.6 \text{ m s}^{-1}$  (negative values indicate southwestward flow; Fig. 1b). Peak southwestward speeds lie between 20- and 50-km range at the sea surface and shift offshore with depth. Beneath 3500-m depth velocities are northeastwards (Fig. 1b, zero-isotach). The mean current is 40 km wider and  $0.2 \text{ m s}^{-1}$  weaker during ASCA than ACT which is likely due to an extreme meander event in July 2017 that pushed the core of the current 200 km away from the coastline.

The velocity structure of the Agulhas Current, and other western boundary currents, maintains cross-stream salinity gradients in subtropical, central, and intermediate waters (Figs. 3a,b). Cross-stream salinity gradients are greatest within TSW and STSW, defined by  $\gamma < 26.4 \text{ kg m}^{-3}$ , and are  $O(10^{-3}) \text{ psu km}^{-1}$  (Fig. 3a). Beneath these surface waters lies SICW. All three form a wedge that slopes southeastwards and reaches  $\sim 900\text{-m}$  depth at 300-km range with salinities over 34.6 psu. The base of this wedge,  $\gamma = 27 \text{ kg m}^{-3}$ , defines the base of the halocline and start of the salinity minima of  $\sim 34.5 \text{ psu}$  (Figs. 3a,b). This layer is  $\sim 1200\text{-m}$  thick, centered at 1400-m depth and defined by neutral densities of  $27\text{--}27.92 \text{ kg m}^{-3}$ . In this layer, fresher Antarctic Intermediate Water (AAIW) lies offshore while AAIW modified by salty Red Sea Water (RSW) is found close to the continental shelf (Beal et al. 2006). Below 2500-m depth, deep waters are laterally homogenous implying that the current has little control on water mass properties at these depths (Beal et al. 2006). A salinity maximum of  $\sim 34.8 \text{ psu}$  is consistent with North Atlantic Deep Water (NADW) that enters the western Indian Ocean around the tip of Africa (Fig. 3b). Our time-mean salinity section interpolated from point measurements (Figs. 3a,b) compares well to in situ hydrographic profiles projected onto the transect (Figs. 3c,d). Hitherto, it has not been possible to quantify hydrographic variability of the Agulhas Current; we now present the leading modes of water mass variability in both depth and density space.

### b. Variability associated with current location

Meanders, mesoscale lateral shifts of the current, drive the largest kinematic variability in the salinity field (EOF1; Figs. 4a,b). EOF1 explains 41% of salinity variance and its principal component time series, PC1 (shown as black line in Fig. 4c), is highly correlated with the meander time series ( $r = -0.8$ ). The meander time series identifies meanders using a sea level anomaly threshold of less than  $-0.2 \text{ m}$  at mooring C (Fig. 4c, red line and gray bands; Elipot and Beal 2015). EOF1 shows that meanders drive the highest salinity variance in the halocline, at depths shallower than 900 m. Within this depth range, subtropical and central water masses have the greatest salinity anomalies at 50–150 km from the coastline (Fig. 4a). Prior to and during a meander, the halocline becomes fresher by up to 0.4 psu (positive phases of PC1; Fig. 4, gray bands). Meanwhile, small yet widespread, increases in salinity of up to 0.05 psu are observed at depths below 1 km (Fig. 4b). During a meander SICW and AAIW shoal by up to 200 m. Shortly after a meander, PC1 becomes negative, while SICW and AAIW deepen by up to 150 m (Fig. 4d, gray bands). Because of the AAIW salinity minimum at 1400-m depth,

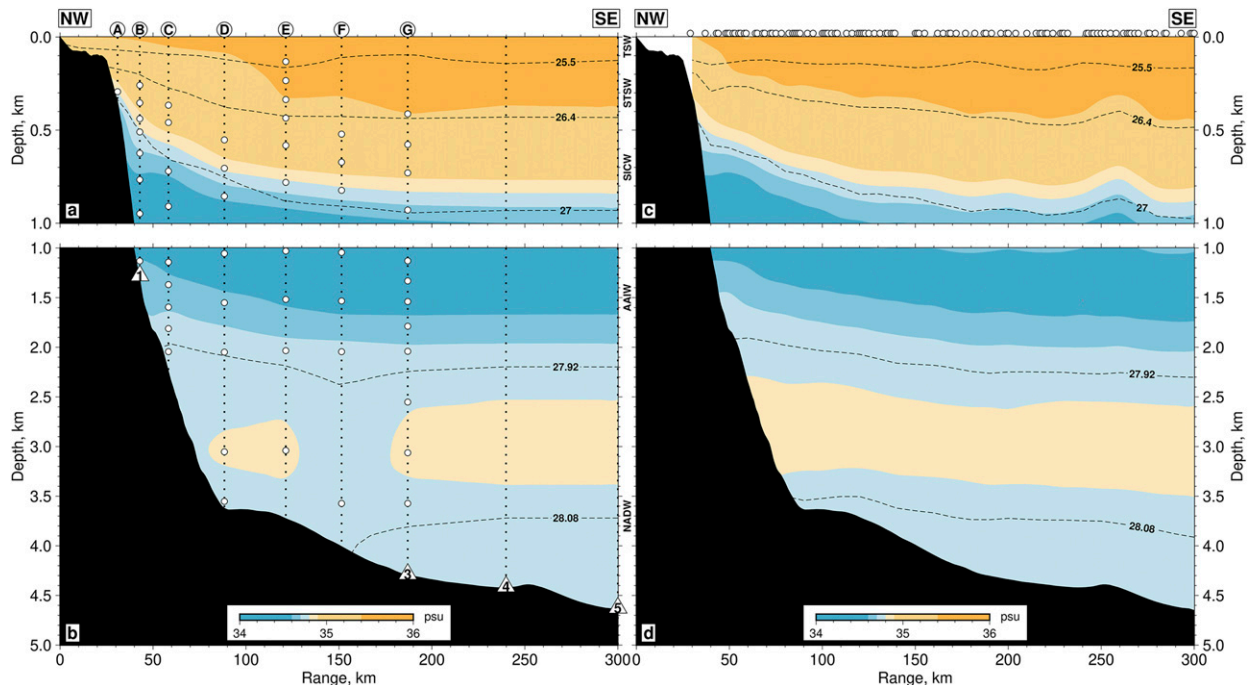


FIG. 3. Time-mean salinity field for ASCA and regional in situ data. Salinity field interpolated from ASCA for (a) 0–1- and (b) 1–5-km depth. Labeled white circles = surface loci of moorings A–G; white triangles = loci of CRIES 1, 3, 4, and 5; white circles = time-mean pressure levels of microCATs; dotted lines = vertical extent of ASCA moorings; dashed black lines = neutral density  $\gamma$  surfaces that define labeled water masses as described in the text; black shading = seabed. Comparison salinity field interpolated from regional in situ data within 50 km of ASCA for (c) 0–1- and (d) 1–5-km depth. White circles = surface loci of hydrographic profiles projected onto the ASCA transect. The other symbols are as in (a) and (b).

shoaling of isopycnals causes freshening above, and an increase in salinity below, this depth (Figs. 2 and 3). The correlation coefficient between the sea level anomaly and depth anomaly time series is 0.9 (Fig. 4d). Therefore, meanders cause vertical uplift of water masses that results in freshening within and above the halocline and salinification below. It is important to note this heave is reversed after the meander passes.

Next, we separate signals of irreversible salinity change from those signals caused by isopycnal heave by conducting an EOF analysis in density space—a measure of variance caused by irreversible processes only (DEOF1). DEOF1 explains 48% of salinity variability and has a correlation coefficient of  $-0.7$  with the meander time series (Fig. 5b, red line). Similar to EOF1, DEOF1 shows two main regions of variability above and below the halocline. During meanders, freshening occurs in water masses STSW and SICW while salinity increases at the SICW–AAIW interface and in upper AAIW (Fig. 5, 25.5–27 and 26.8–27.3  $\text{kg m}^{-3}$ ). These opposing salinity anomalies are quasi-vertically aligned across the SICW–AAIW interface implying diapycnal mixing (Fig. 5a, 27  $\text{kg m}^{-3}$ ). This inference is supported by thickness anomalies of SICW and AAIW that show that, during meanders, the former thins while the latter thickens (Fig. 5c). The correlation coefficient of the thickness anomalies of SICW and AAIW is  $-0.7$  while they are negligibly correlated with water mass thicknesses directly above and below, suggesting that exchange is limited to SICW and AAIW. We conclude that diapycnal mixing is

occurring between central and intermediate waters during meanders.

Our results are consistent with Leber and Beal (2015), who found that, during a single meander, 0.25 psu of freshening and  $1^\circ\text{C}$  of cooling occurred above the thermocline with salinification and warming of the same magnitude below. We are able to expand upon their results in three ways. First, upwelling and, critically, diapycnal mixing occurs during all meanders observed during ASCA suggesting that these processes are common, if not ubiquitous. Second, while heave occurs fairly uniformly across the halocline, diapycnal mixing is found preferentially at 60–120-km range. This range is the mean location of the inshore flank of the current after shifting offshore during meanders. In the Gulf Stream, intense diapycnal mixing has been found at the flanks of meanders due to frontogenic processes, specifically enhanced vertical shear (Rodríguez-Santana et al. 1999). Yet, because of the vertical spacing between instruments, it is difficult to determine the exact mechanisms driving the enhanced diapycnal mixing at this location. We note that this distance offshore is around the foot of the continental slope (Fig. 1b). It is unlikely that tides play a significant role in mixing of the Agulhas Current, since their amplitudes, of  $O(0.01) \text{ m s}^{-1}$ , are two orders of magnitude less than the current itself. Third, we find that smaller, submesoscale lateral shifts of the current also drive reversible and irreversible variability in the salinity field. Submesoscale anomalies, defined here as lateral shifts of the current of

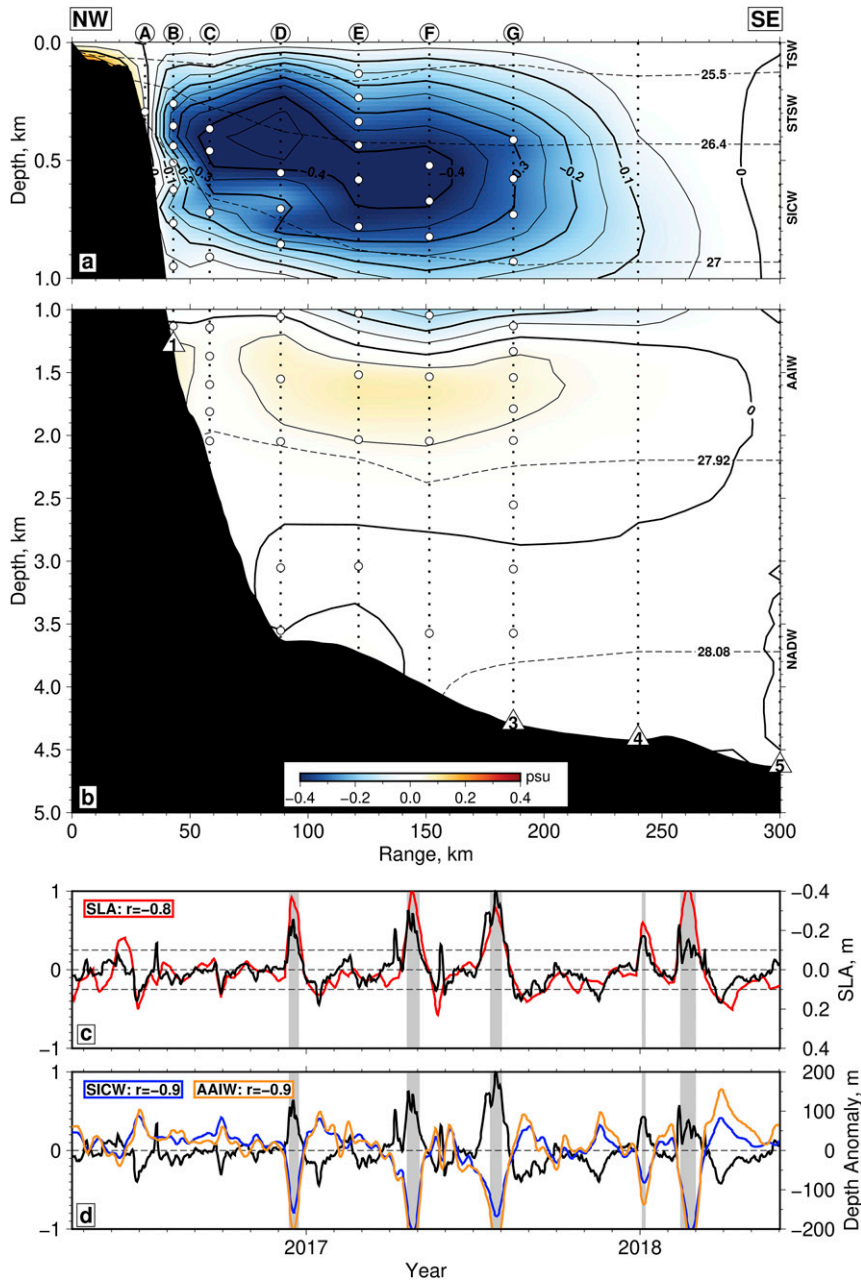


FIG. 4. Dominant mode of variability of salinity field calculated in depth space, EOF1: (a) Space-dependent pattern of EOF1 between 0- and 1-km depth. Red and blue shading = positive and negative salinity anomaly, respectively; solid black lines = salinity anomaly contours every 0.05 psu; labeled white circles = surface loci of moorings A–G; white triangles = loci of CPIES 1, 3, 4, and 5; white circles = time-mean pressure levels of microCATs; dotted lines = vertical extent of ASCA moorings; black dashed lines = neutral density surfaces; black shading = seabed. (b) EOF1 between 1- and 5-km depth. The symbols are as in (a). (c) Time-dependent amplitude of EOF1, PC1. Solid black line and left axis = PC1; red line and right axis = sea level anomaly, SLA; gray boxes = meander periods; red box =  $r$  between time series. (d) Middepth anomalies of SICW and AAIW at 120-km range (negative values indicate shoaling). Blue line and right axis = SICW; orange line and right axis = AAIW. The other symbols are as in (c).

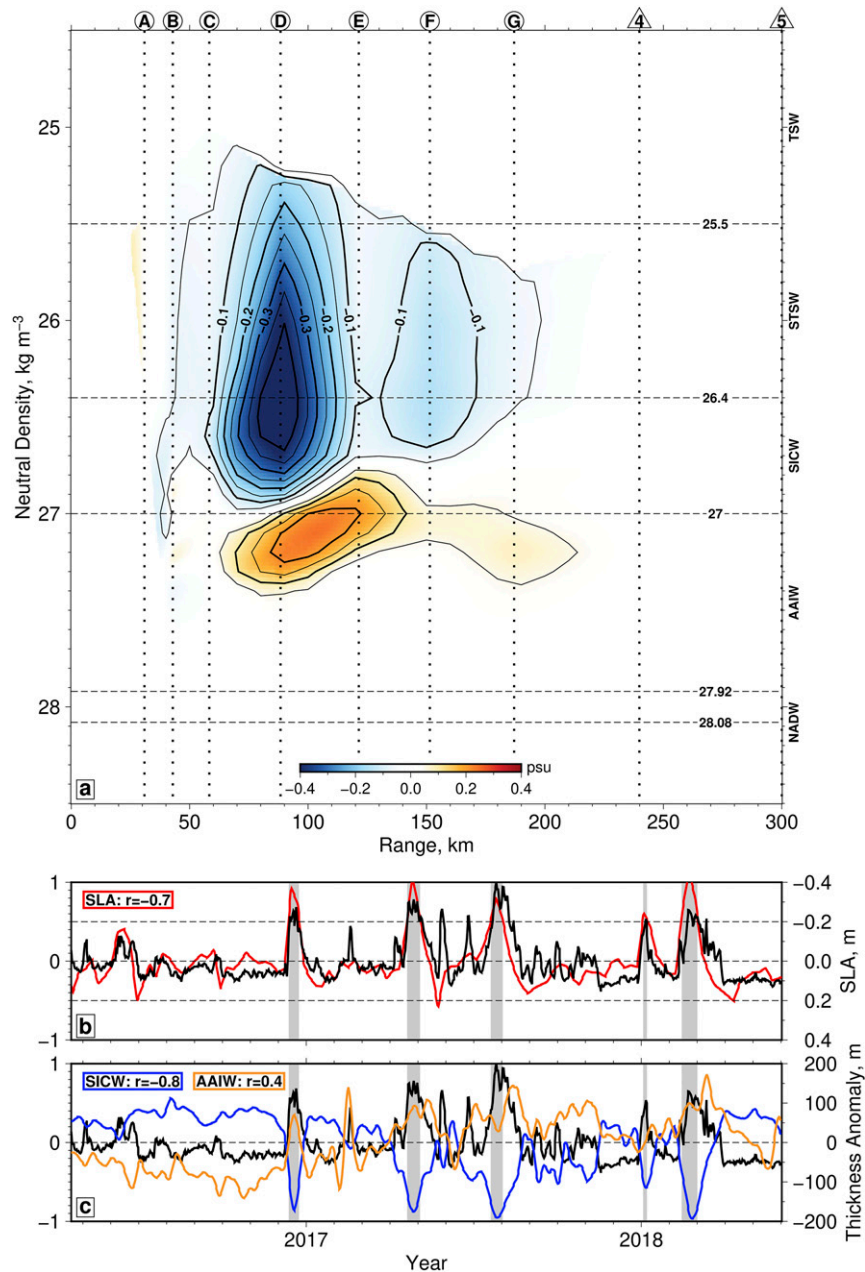


FIG. 5. Dominant mode of variability of salinity field calculated in density space, DEOF1: (a) Space-dependent pattern of DEOF1. Red and blue shading = positive and negative salinity anomaly, respectively; solid black lines = contours of salinity anomaly every 0.05 psu; labeled white circles = surface loci of moorings A–G; white triangles = loci of CRIESs 4 and 5; dotted lines = vertical extent of ASCA moorings; black dashed lines = neutral density surfaces. (b) Time-dependent amplitude of DEOF1, DPC1. Solid black line and left axis = DPC1; red line and right axis = sea level anomaly, SLA; gray boxes = meander periods; red box =  $r$  between time series. (c) Thickness anomalies of water masses at 90-km range (negative values indicate thinning). Blue line and right axis = SICW; orange line and right axis = AAIW. The other symbols are as in (b).

$\leq 50$  km, result in salinity anomalies of  $O(0.1)$  psu (e.g., see August–November 2017 of Figs. 4 and 5). We find that, in a given year, PC1 and DPC1 are associated with salinity anomalies of over 0.1 psu for 111 days of the year. Meanders drive salinity

anomalies of up to 0.4 psu and are present for 43 days of the year. Hence, submesoscale meandering of the current—shifts that do not involve full separation of the current from the continental slope—are important drivers of subsurface salinity



variability. It is important to note that this scale of variability is not easily observed from space. When the current shifting is small, isopycnals do not outcrop and upwelling and mixing is cryptic, that is, occurring below the surface. Indeed, [Leber et al. \(2017\)](#) speculated that their reliance on satellite data meant many upwelling events were undetected, and [Goschen et al. \(2012\)](#) observed that subsurface upwelling events over the shelf are much more frequent than surface events.

### c. Variability associated with current strength

Changes in along-stream jet strength (i.e., current pulsing) drive salinity variability via changes in isopycnal slope associated with geostrophic adjustment. This mode of variability is described by EOF2, which explains 25% of total salinity variance. Isopycnals flatten when the current is weak; when the strength of the jet is less than 48 Sv, SICW deepens close to the continental shelf by up to 100 m ([Fig. 6d](#), orange line) while shoaling in offshore regions ([Fig. 6d](#), blue line). Hence, when the current weakens there is: (i) salinification of +0.3 psu between 35- and 120-km range and (ii) freshening of -0.25 psu at ranges over 200 km ([Fig. 6](#)). During strong pulses, when the southwestward strength of the jet is greater than 100 Sv, PC2 becomes negative and there is freshening of the current. These salinity anomalies are primarily constrained to subtropical (STSW) and central (SICW) water masses.

EOF analysis in density space (DEOF2) isolates irreversible changes associated with current pulsing and isopycnal heave ([Fig. 7](#)). These anomalies explain 14% of variance and up to 0.2 psu of the total signal. Salinity anomalies are aligned along  $\gamma = 26.4 \text{ kg m}^{-3}$  implying along-isopycnal mixing. This inference is supported by the high correlation of this mode with changes in slope of subtropical and central water masses. We calculate the isopycnal slope anomaly,  $\Delta dp/dx$ , for SICW between moorings B and F ([Fig. 7c](#)). During weak pulses, isopycnals flatten and water masses move closer to horizontal, indicated by positive  $\Delta dp/dx$ , and we observe (i) salinification of up to +0.2 psu at 40–90-km range and (ii) freshening of -0.15 psu at ~150-km range ([Figs. 7b,c](#)). These anomalies are centered on the interface between subtropical and central waters where the background salinity increases from 35 to 35.5 psu from onshore to offshore ([Fig. 2c](#)). Thus, current pulsing causes irreversible variability in the form of cross-stream along-isopycnal mixing of haloclinic waters.

Salinity anomalies related to cross-stream mixing are sharply attenuated between moorings A and B—the time-mean position of the jet core ([Fig. 7](#), 30–40-km range). This spatial limit of variability is likely caused by the jet's large cross-stream potential vorticity gradient and kinematic steering that inhibit cross-frontal mixing ([Beal et al. 2006](#)). Therefore, current pulsing drives cross-stream mixing within the anticyclonic flank of the jet and there is no evidence of cross-frontal exchange of waters from the anticyclonic to the cyclonic side of the jet.

We have found that even small changes in the location and strength of the Agulhas Current at 34°S drive water mass mixing across and along isopycnals, respectively. Farther

downstream, at the Agulhas Bank Bight, where eddy kinetic energy increases in the Agulhas Current, we speculate there may be more diapycnal and cross-stream mixing. The Agulhas Bank hosts an important nursery and spawning area, thus diapycnal and cross-stream fluxes likely influence biological productivity here ([Hutchings 1994](#); [Hutchings et al. 2002](#)) and could be investigated in future research.

### d. Transport variability

Following [Beal et al. \(2015\)](#), we define box and jet transport to reveal variability of the Agulhas Current in fixed and streamwise frames of reference, respectively. The time-mean and standard deviation of box transport  $T_{vb}$  are -75 and 26 Sv ([Fig. 8a](#), red line), and for jet transport  $T_v$  the values are -76 and 22 Sv ([Fig. 8a](#), black line). The transport of the Agulhas jet is largely maintained during meanders while the box transport reduces as a result of strong inshore countercurrents ([Leber and Beal 2014](#)). However, during ASCA, three meanders forced portions of the Agulhas Current offshore and outside the range of the array, resulting in decreased  $T_v$ . Overall, the mean transport of the Agulhas Current during ASCA is consistent with results from ACT; however, long-term monitoring of the Agulhas Current is required to determine robust inter-annual and decadal variability ([Table 1](#); [Beal and Elipot 2016](#); [Morris et al. 2017](#)).

The salt transport of the Agulhas Current is a significant component of the Indian Ocean's freshwater budget. We find its salt transport  $T_s$  has a time-mean of -2650 Sv psu, whereas the Indonesian Throughflow—the current connecting the Pacific Ocean to the Indian Ocean—has a salt transport of 520 Sv psu based on a time-mean volume transport of 15 Sv and salinity of 34.73 psu ([Table 1](#); [Sprintall et al. 2009](#); [Wijffels et al. 2008](#)). The standard deviation of Agulhas Current salt transport is large, 770 Sv psu or 30% of the mean. The Indonesian Throughflow salt transport is an order of magnitude lower than that of the Agulhas Current and is less than its variability ([Fig. 8b](#), cf. pink and white circles).

The ratio of volume to salt transport, known as transport-weighted salinity, provides an indicator of how water properties within the jet affect changes in salt transport independent of changes in velocity ([Fig. 8c](#)). Its range is 34.82–35.37 psu. The time-mean and standard deviation are 35.02 and 0.05 psu, respectively. Salinity of 35.02 psu is indicative of SICW—the main halocline water mass ([Fig. 2](#)). When compared with the Indonesian Throughflow and interior ocean, the Agulhas Current is saltier ([Wijffels et al. 2008](#); [Hernández-Guerra and Talley 2016](#)).

Using our results described above we can estimate salt leakage into the Atlantic Ocean. Agulhas leakage is important for its influence on the Atlantic overturning circulation ([Beal et al. 2011](#)), yet its salt flux is poorly defined, particularly outside Agulhas rings. Recently, [Daher et al. \(2020\)](#) used a large observational dataset, composed of Argo floats and drifters, to update the seminal leakage estimate of [Richardson \(2007\)](#). They found that 28% of the Agulhas Current leaks into the Atlantic. Combined with our 2016–18 time-mean volume transport  $\overline{T}_v = 76 \text{ Sv}$ , 21 Sv of Indian Ocean water leaks into the Atlantic on average. Assuming divergence of salt is small

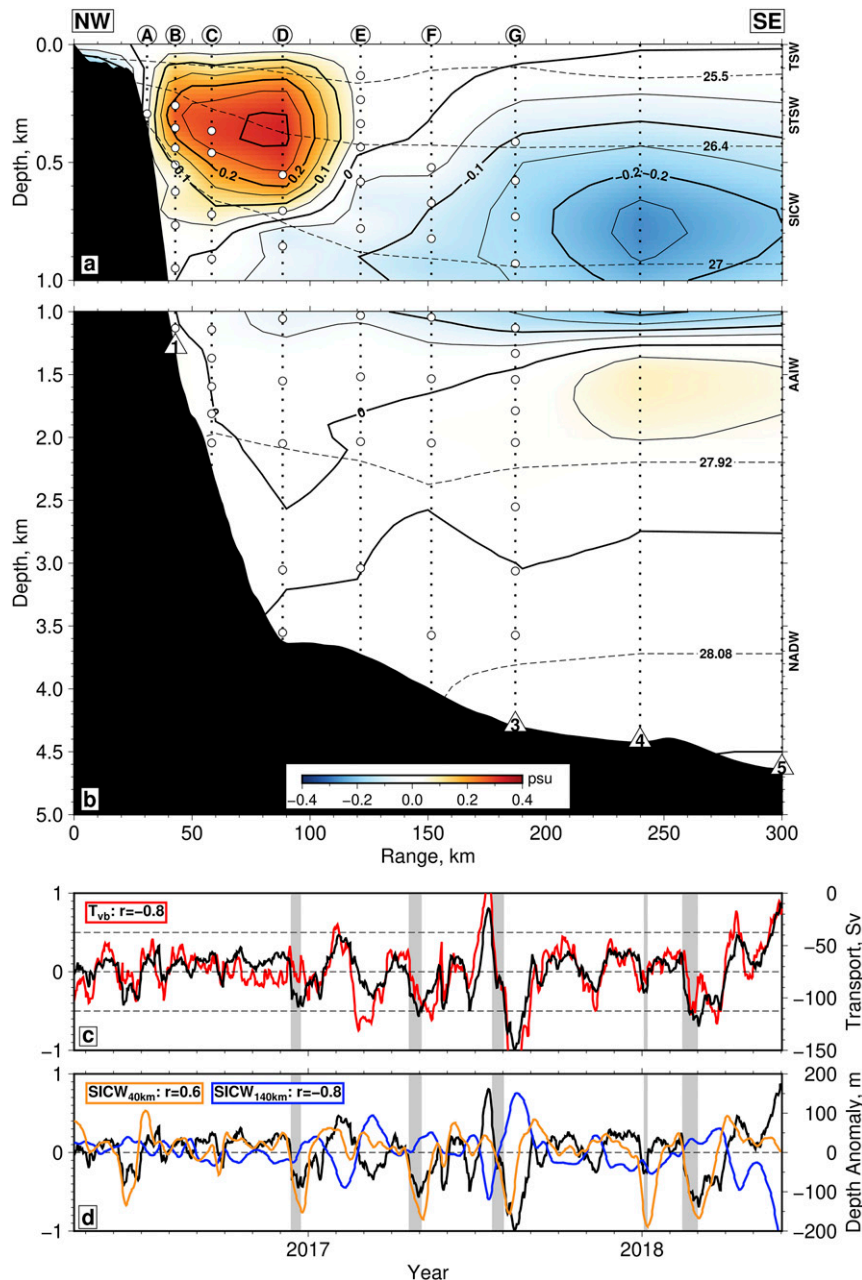


FIG. 6. Second mode of variability of salinity field calculated in depth space, EOF2: (a) Space-dependent pattern of EOF2 between 0- and 1-km depth. Red and blue shading = positive and negative salinity anomaly, respectively; solid black lines = contours of salinity anomaly every 0.05 psu. labeled white circles = surface loci of moorings A–G; white triangles = loci of CPIPEs 1, 3, 4, and 5; white circles = time-mean pressure levels of microCATs; dotted lines = vertical extent of ASCA moorings; black dashed lines = neutral density surfaces; black shading = seabed. (b) EOF2 between 1- and 5-km depth. The symbols are as in (a). (c) Time-dependent amplitude of EOF2, PC2. Solid black line and left axis = PC2; red line and right axis = volume transport time series calculated using box definition ( $T_{vb}$ ); gray boxes = meander periods; red boxes =  $r$  between time series. (d) Middepth anomalies of SICW (negative values indicate shoaling). Orange line and right axis = middepth anomaly of SICW at 40-km range; blue line and right axis = middepth anomaly of SICW at 140-km range. The other symbols are as in (c).

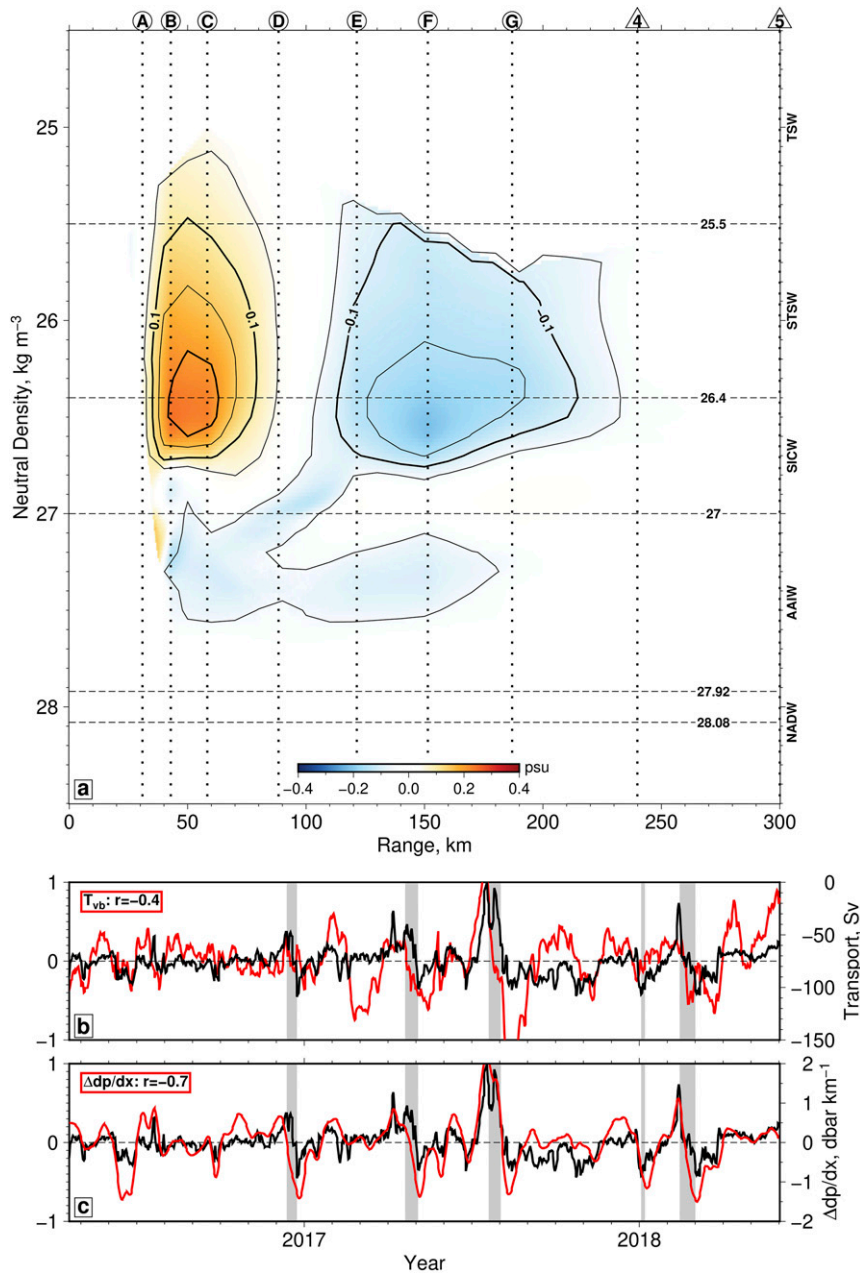


FIG. 7. Second mode of variability of salinity field calculated in density space, DEOF2: (a) Space-dependent pattern of DEOF2. Red and blue shading = positive and negative salinity anomaly, respectively; solid black lines = contours of salinity anomaly every 0.05 psu; labeled white circles = surface loci of moorings A–G; white triangles = loci of CPIES 4 and 5; dotted lines = vertical extent of ASCA moorings; black dashed lines = neutral density surfaces. (b) Time-dependent amplitude of DEOF2, DPC2. Solid black line and left axis = DPC2; red line and right axis =  $T_{vb}$ ; gray boxes = meander periods; red box =  $r$  between time series. (c) Anomaly of isopycnal slope  $dp/dx$  of SICW measured between moorings A and F,  $\Delta dp/dx$ . Solid black line = DPC2; red line and right axis =  $\Delta dp/dx$  (positive values indicate flattest slope); red box =  $r$  between time series.

between 34°S and the retroflection, we calculate the salinity difference,  $dS$ , between Agulhas waters from ASCA and South Atlantic water (from BEST; Garzoli and Gordon 1996) then vertically average over 2000 m depth. Based on these values,

we estimate that  $8 \times 10^{13}$  kg yr<sup>-1</sup> of salt is added on average to the Atlantic Ocean. This estimate can be considered a measure of the total leakage salt flux including the background flow as well as Agulhas rings. Our estimate is consistent with

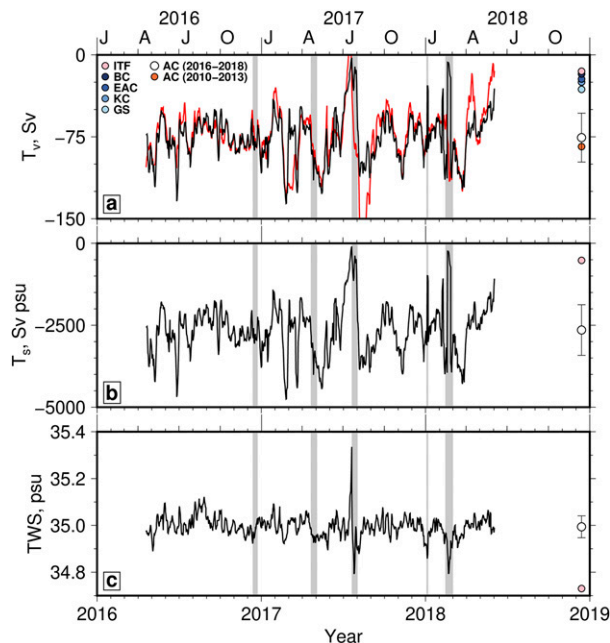


FIG. 8. Time series of fluxes across ASCA transect: (a) Volume transport. Solid black and red lines = calculated  $T_v$  and  $T_{vb}$  time series, respectively, at 20-h intervals; blue circles = available estimates of time-mean  $T_v$  in other western boundary currents (BC = Brazil Current; EAC = East Australian Current; KC = Kuroshio; GS = Gulf Stream; Stramma 1989; Qiu 2001; McDonagh et al. 2015; Sloyan et al. 2016); pink circle = 20-yr time-mean transport of Indonesian Throughflow (ITF; Sprintall et al. 2009); orange circle = time mean between 2010 and 2013 measured in Agulhas Current (AC; Beal et al. 2015); white circle = time mean and standard deviation of  $T_v$  in AC between 2016 and 2018; gray bands = meander periods. (b) Salt transport. Solid black line = calculated  $T_s$  time series at 20-h intervals for jet-defined current. Pink circle = ITF salt transport based on time-mean volume and salinity (Sprintall et al. 2009; Wijffels et al. 2008). (c) Transport-weighted salinity. Solid black line = calculated time series at 20-h intervals for jet-defined current. Pink circle = ITF transport-weighted salinity (Wijffels et al. 2008).

observations of ring advection as well as recent modeling efforts (van Ballegooyen et al. 1994; McDonagh et al. 1999; Biastoch et al. 2015). It is important to note that increasing  $dS$  by the standard deviation of transport-weighted salinity 0.05 psu, while maintaining  $\bar{T}_v$ , increases leakage salt flux by an order of magnitude. Thus, Agulhas leakage salt flux is highly sensitive to upstream water mass variability.

#### 4. Summary

ASCA successfully measured 26 months of Agulhas Current velocity, temperature, and salinity variability (Figs. 1–3). Here, by analyzing the spatiotemporal variability of salinity—a tracer of water masses—we have learned how and why water masses vary within the current, distinguishing reversible (i.e., heave) from irreversible (i.e., mixing) variability.

Current shifting, changes in location, and pulsing, changes in strength, drives local salinity variability through heave and

TABLE 1. Statistics of time series for  $T_v$ ,  $T_s$ , and transport-weighted salinity.

	$T_v$ (Sv)	$T_s$ (Sv psu)	Transport-weighted salinity (psu)
Mean $\pm$ std error	$-76 \pm 11$	$-2650 \pm 130$	$35.02 \pm 0.05$
Std dev	22	770	0.05
Max	-3	-94	35.37
Min	-134	-4752	34.82
Dec–Feb mean	-75	-2611	34.98
Jun–Sep mean	-68	-2385	35.01

mixing. These changes in subtropical, central, and intermediate waters are associated with water mass changes along isopycnals, heave of up to 200 m and thickness changes of up to 150 m (Figs. 4c,d and 5b,c). The latter is evidence of diapycnal mixing, which accounts for a large portion of total salinity variance.

Mesoscale shifts (i.e., meanders) drive the greatest salinity anomalies. These shifts of the current cause order 0.4 psu of freshening in STSW and SICW while AAIW gains up to 0.25 psu of salt (Figs. 4a,b and 5a). Based on the average 12-day lifetime of meanders, water masses may ascend by up to  $17 \text{ m day}^{-1}$  and thin/thicken by  $12.5 \text{ m day}^{-1}$  (Figs. 4d and 5c). This ascent has been found to lift water onto the continental shelf and displace surface waters offshore, creating larval population sinks and dispersing inshore pollutants (Churchill et al. 1986; Porri et al. 2014). Clearly, meanders have the most significant impact on the water column. Yet, we find that submesoscale shifts of the current also have irreversible impacts and are active for a greater portion of the year, 111 days, as compared with 43 days of meandering. Hence, submesoscale shifts of the current may have as much impact on subsurface water properties as meanders and should not be overlooked even though they are not observable via satellite.

Current pulsing causes changes in the depth and slope of the halocline in keeping with geostrophic balance. During weak transport anomalies, salinification and freshening of the near-shore and offshore halocline of up to 0.3 psu occurs as the isopycnals flatten (Fig. 6). During transport pulses, the pattern of near- and offshore anomalies is reversed. Meanwhile, the change in isopycnal slope encourages cross-stream mixing (Fig. 7). This mixing is focused along the subtropical–central water mass interface and results in irreversible salinity anomalies of up to 0.2 psu.

The mean volume and salt transport of the Agulhas Current from 2016 to 2018 are  $-76 \text{ Sv}$  and  $-2650 \text{ Sv psu}$ , respectively, with total uncertainties of  $\pm 11 \text{ Sv}$  and  $\pm 130 \text{ Sv psu}$ . The salt transport of the Agulhas Current is an order of magnitude greater than the Indonesian Throughflow. The salt flux into the Atlantic is estimated to be of  $O(10^{13}) \text{ kg yr}^{-1}$  and, critically, can vary by an order of magnitude as a result of changes in the Agulhas Current transport-weighted salinity alone. Our results confirm that the Agulhas Current dominates the freshwater budget of the Indian Ocean.

*Acknowledgments.* This work was funded by NSF Award 1459543 as part of the Agulhas System Climate Array. We thank the crews of the RS *Algoa* and SA *Agulhas* as well as Bradley Blows and Nauti-Buoys for building the ASCA moorings and leading deck operations on deployment and recovery. Special thanks are given to D. Murphy for his patient writing advice. We acknowledge the support of the South African Department of Science and Innovation and the National Research Foundation of South Africa through the South African Environmental Observation Network (SAEON), and the Department of Environment, Forestry and Fisheries (DEFF, Branch: Oceans and Coasts).

*Data availability statement.* Hydrographic data are freely available from the World Ocean Database ([https://www.nodc.noaa.gov/OC5/WOD/pr\\_wod.html](https://www.nodc.noaa.gov/OC5/WOD/pr_wod.html)). These measurements were analyzed using MATLAB implementation of GSW TEOS-10 ([github.com/TEOS-10/GSW-Matlab](https://github.com/TEOS-10/GSW-Matlab)). Drifter-Derived Climatology of Global Near-Surface Currents is available online ([https://www.aoml.noaa.gov/phod/gdp/mean\\_velocity.php](https://www.aoml.noaa.gov/phod/gdp/mean_velocity.php); Laurindo et al. 2017). Bathymetry contours are from the International Bathymetric Chart of the Southern Ocean (<https://doi.pangaea.de/10.1594/PANGAEA.805734>; Arndt et al. 2013). Along-track sea-level anomaly data are available online (<https://marine.copernicus.eu>). Figures were prepared using Generic Mapping Tools ([gmt.soest.hawaii.edu](https://gmt.soest.hawaii.edu)). Individual instrument records (current meters, microCATs, and CPIES) collected during ASCA are available at [accession.nodc.noaa.gov/0209237](https://accession.nodc.noaa.gov/0209237) and [accession.nodc.noaa.gov/0210643](https://accession.nodc.noaa.gov/0210643). Gridded temperature, salinity, and velocity fields are available online (<https://beal-agulhas.rsmas.miami.edu/data-and-products>). The BEST data are available online (<https://cchdo.ucsd.edu/cruise/74DI202>).

## APPENDIX

### Derivation of Errors

ASCA time-mean salinity fields compare well to historical in situ hydrographic data that have been projected onto the array as well as earlier collocated measurements. Regardless, it is necessary to quantify the uncertainty created through the collection and processing of data presented here. There are three types of error associated with this experiment: (i) sampling error, (ii) instrumental error, and (iii) a second type of sampling error that we call “missing data.” The missing-data error is caused by the loss of velocity measurements partway through the experiment, and we treat them separately. The errors calculated here are conservative and are primarily associated with CPIES.

#### a. Salinity

Sampling and instrumental errors are combined in quadrature to produce a total estimate of salinity uncertainty. First, we estimate salinity sampling errors by comparing gridded fields derived from (i) an entire hydrographic transect and (ii) the same set of measurements subsampled to match ASCA instrument spacing. We use three hydrographic transects collected in 2010, 2011, and 2013 as part of the ACT experiment,

because they are collocated with ASCA (Beal et al. 2015; Leber and Beal 2015). All CTD profiles collected during one survey are horizontally linearly interpolated to provide a salinity section. We consider this section to be the most accurate representation of water mass properties at that time. The same CTD data are then subsampled at the mean depths and locations of each microCAT, and a new salinity section is reconstructed following the same gridding procedure described in section 1. We calculate the horizontally averaged root-mean-square error (RMSE) between the true and reconstructed fields to estimate the sampling error of salinity. The final, depth-dependent sampling error is taken as the average of the RMSE profiles derived from each of the three hydrographic sections. Sampling errors are greatest in the upper 500 m where there are the least number of instruments. At the surface, the sampling error is 0.1 psu. At 500-m depth the error has decreased to 0.05 psu (Fig. A1a, yellow line). It is important to note that the sampling error estimate is calculated after recovering the near-surface salinity using satellite measurements, therefore quantifies the uncertainty associated with this method. When sea surface measurements are not used and the salinity is rather interpolated upward from the shallowest microCAT, the near-surface sampling error increases by 40%, to 0.14 psu. The increase in uncertainty is due to the shallow vertical structure of salinity that is not captured by the microCATs, and therefore sea surface salinities are overestimated. Therefore, including sea surface measurements improves the derived salinity grid [as also found for temperature by McMonigal et al. (2020)].

Bias in the salinity measurements may be caused by the low number of microCATs in the upper water column. By comparing a contemporaneous hydrographic section collected during the ASCA experiment (July 2016; Hermes et al. 2020) with the gridded fields, as described above, we assess the existence of biases. We find that the gridded fields are too fresh, which is likely related to the shallow subsurface salinity maxima that is not captured by this experiment. The full-depth salinity bias is 0.03 psu and is included in the final error estimate.

Second, instrumental errors are determined. Instrumental errors for microCATs are negligible, of  $O(0.001-0.01)$ , when compared with sampling errors; therefore, we do not consider them further. A nonnegligible CPIES instrumental (or methodological) error arises from the ability of the GEM to resolve the water column. This methodological error is estimated at each depth by considering the residuals between input data and the GEM function fit (Fig. A1a, red line; Donohue et al. 2010).

Last, the sampling and instrumental errors, as well as the salinity bias, are combined in quadrature to produce a total estimate of salinity error (Fig. A1a, black line). Salinity errors are largest near the surface, reaching almost 0.15 psu. At 2000-m depth, the errors have decreased by an order of magnitude. The depth-averaged salinity error is 0.05 psu.

#### b. Velocity

Sampling, instrumental, and missing-data errors are combined in quadrature to produce a total estimate of velocity uncertainty. First, we estimate the sampling errors. A sampling

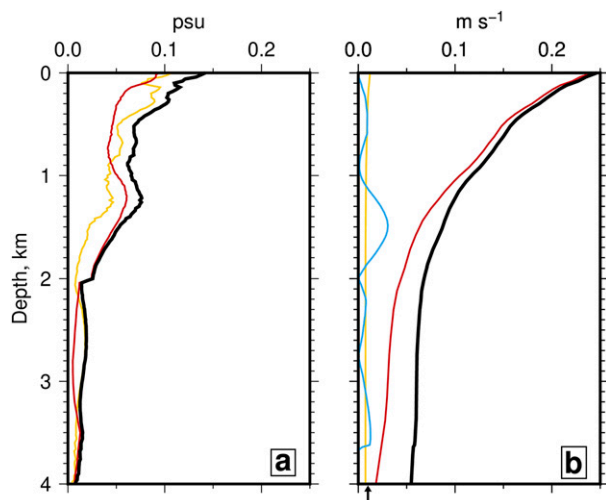


FIG. A1. Errors associated with ASCA: (a) Salinity errors as function of depth. Yellow line = sampling error from microCATs and CPIES; red line = methodological error from CPIES; thick black line = total salinity error. (b) Velocity errors as function of depth. Yellow line = CM sampling error; red line = CPIES sampling error; blue line = missing-data error; black arrow = instrument error; thick black line = total velocity error.

error for CPIES was previously calculated for the ACT experiment (Fig. 5e of Beal et al. 2015). Since the instrument deployment of CPIES between ACT and ASCA was the same, we use this predicted sampling error (Fig. A1b, red line). By using the predicted error of Beal et al. (2015), we are confident that these uncertainties are representative of the ASCA experiment. Maximum error values of  $0.25 \text{ m s}^{-1}$  occur at the surface, because of the deseasoning of the lookup table, and decrease to  $\sim 0.01 \text{ m s}^{-1}$  at 4000 m. For CMs and ADCPs, sampling error is estimated using the method of Johns et al. (2005) as in Beal et al. (2015). The greatest errors are also found in the upper water column and have maximum values of  $0.02 \text{ m s}^{-1}$  (Fig. A1b, yellow line).

Second, the instrument errors are assessed. Nominal instrument accuracy of CMs and ADCPs is given by the manufacturer. However, this error is likely to be larger than quoted values because of the heterogeneity of the devices. Therefore, instrument errors are estimated using power spectra of the individual velocity measurements as described in Beal et al. (2015). The median value from all instruments of  $0.01 \text{ m s}^{-1}$  is chosen. This error is of a similar order to sampling errors; therefore, we include it in our final estimate (Fig. A1b, black arrow).

Last, the missing-data error associated with shortened velocity time series is estimated by comparing gridded fields derived from (i) a complete set of velocity time series and (ii) the same records but shortened to match the recovery of ASCA. A true velocity section is constructed using the ACT velocity time series, which benefited from excellent data coverage (Beal et al. 2015). The ACT velocity time series are then shortened to match the recovery of CMs and ADCPs during ASCA (Fig. 1b, red, orange, and yellow squares). The

horizontally averaged RMSE profile, between the true and shortened datasets, has largest errors near 1500-m depth where the lowest data coverage occurred (Fig. A1b, blue line).

The sampling, instrument, and missing-data errors are combined in quadrature to produce a total estimate of velocity error (Fig. A1b, black line). This error profile is dominated by uncertainties associated with CPIES, and the depth-averaged velocity error is  $0.1 \text{ m s}^{-1}$ .

### c. Transport

Our measurements of  $T$ ,  $S$ , and  $v$  are ultimately used to calculate property fluxes across ASCA, therefore we estimate their uncertainties (temperature variability discussed in McMonigal et al. 2020). The error for each 20-h estimate is derived following the method of McDonagh et al. (2015) by combining salinity- and transport-derived errors. The transport-derived error is the product of volume transport uncertainty  $\sigma_{T_v}$  and depth-averaged salinity. Jet volume transport errors derivation contain many steps discussed in detail in Beal et al. (2015). Applying the same procedure, we estimate the jet volume transport error  $\sigma_{T_v}$  as 14.6 Sv during ASCA. Based on this value and a depth-averaged salinity of 34.8 psu, the transport-derived error is 510 Sv psu. Next, we calculate the salinity-derived uncertainty as the product of salinity uncertainty (0.05 psu) and the time-mean jet volume transport (76 Sv). The salinity-derived uncertainty is 4 Sv psu and is negligible relative to the transport-derived error. Combined in quadrature, the total estimated salt transport error for each 20-h record is 510 Sv psu.

Our estimates of the instantaneous errors for volume and salt transport are consistent in magnitude with simpler estimates obtained by spatially integrating the total error profiles of Fig. A1 over the depth-dependent width of the current. For volume and salt transport the values found in this way are 5 Sv and 170 Sv psu, respectively. Both values are smaller than the estimated errors calculated previously, 14.6 Sv and 510 Sv psu, which are conservative upper bound errors for each 20-h record (Beal et al. 2015).

The estimated transport errors on the mean are found by dividing the 20-h estimates by the square root of the degrees of freedom  $N$  (Emery and Thomson 2014). For volume and salt transport  $N$  is 97 and 86 (based on estimated decorrelation time scales of each time series), giving 9 Sv and 50 Sv psu, respectively. These estimated errors are combined with the standard error of the mean, or statistical error, which accounts for the ability of a time series to quantify a mean. The statistical error is the standard deviation of each time series divided by  $N^{1/2}$  and is 2 Sv and 80 Sv psu for volume and salt transport, respectively. Following Kanzow et al. (2010) and Beal et al. (2015), we define the total error as the linear addition of the estimated and statistical errors. Thus, the total mean errors for volume and salt transport are 11 Sv and 130 Sv psu.

We correct the salt transport and transport-weighted salinity time series for the fresh bias (this appendix, section a). The total salt transport and transport-weighted salinity biases are 3 Sv psu (i.e.,  $0.03 \text{ psu} \times 76 \text{ Sv}$ ) and 0.03 psu, respectively. These values are added at each point in time to the time series to correct for the bias.

## REFERENCES

- Arndt, J. E., and Coauthors, 2013: The International Bathymetric Chart of the Southern Ocean (IBCSO) version 1.0—A new bathymetric compilation covering circum-Antarctic waters. *Geophys. Res. Lett.*, **40**, 3111–3117, <https://doi.org/10.1002/grl.50413>.
- Beal, L. M., and S. Elipot, 2016: Broadening not strengthening of the Agulhas current since the early 1990s. *Nature*, **540**, 570–573, <https://doi.org/10.1038/nature19853>.
- , T. K. Chereskin, Y. D. Lenn, and S. Elipot, 2006: The sources and mixing characteristics of the Agulhas current. *J. Phys. Oceanogr.*, **36**, 2060–2074, <https://doi.org/10.1175/JPO2964.1>.
- , and Coauthors, 2011: On the role of the Agulhas system in ocean circulation and climate. *Nature*, **472**, 429–436, <https://doi.org/10.1038/nature09983>.
- , S. Elipot, A. Houk, and G. M. Leber, 2015: Capturing the transport variability of a western boundary jet: Results from the Agulhas Current Time-Series Experiment (ACT). *J. Phys. Oceanogr.*, **45**, 1302–1324, <https://doi.org/10.1175/JPO-D-14-0119.1>.
- Biastoch, A., C. W. Böning, J. Getzlaff, J. Molines, and G. Madec, 2008: Causes of interannual-decadal variability in the meridional overturning circulation of the midlatitude North Atlantic Ocean. *J. Climate*, **21**, 6599–6615, <https://doi.org/10.1175/2008JCLI2404.1>.
- , J. V. Durgadoo, A. K. Morrison, E. Van Sebille, W. Weijer, and S. M. Griffies, 2015: Atlantic multi-decadal oscillation covaries with Agulhas leakage. *Nat. Commun.*, **6**, 10082, <https://doi.org/10.1038/ncomms10082>.
- Bower, A. S., H. T. Rossby, and J. L. Lillibridge, 1985: The Gulf Stream—Barrier or blender? *J. Phys. Oceanogr.*, **15**, 24–32, [https://doi.org/10.1175/1520-0485\(1985\)015<0024:TGSOB>2.0.CO;2](https://doi.org/10.1175/1520-0485(1985)015<0024:TGSOB>2.0.CO;2).
- Boyer, T. P., and Coauthors, 2018: World Ocean Database 2018. NOAA Atlas NESDIS 87, 207 pp.
- Bryden, H. L., L. M. Beal, and L. M. Duncan, 2005: Structure and transport of the Agulhas Current and its temporal variability. *J. Oceanogr.*, **61**, 479–492, <https://doi.org/10.1007/s10872-005-0057-8>.
- Campos, E. J., D. Velhote, and I. C. Da Silveira, 2000: Shelf break upwelling driven by Brazil current cyclonic meanders. *Geophys. Res. Lett.*, **27**, 751–754, <https://doi.org/10.1029/1999GL010502>.
- Churchill, J. H., P. C. Cornillon, and G. W. Milkowski, 1986: A cyclonic eddy and shelf-slope water exchange associated with a Gulf Stream warm-core ring. *J. Geophys. Res.*, **91**, 9615, <https://doi.org/10.1029/JC091iC08p09615>.
- Daher, H., L. M. Beal, and F. U. Schwarzkopf, 2020: A new improved estimation of Agulhas leakage using observations and simulations of Lagrangian floats and drifters. *J. Geophys. Res. Oceans*, **125**, e2019JC015753, <https://doi.org/10.1029/2019JC015753>.
- Donohue, K. A., D. R. Watts, K. L. Tracey, A. D. Greene, and M. Kinnally, 2010: Mapping circulation in the Kuroshio extension with an array of current and pressure recording inverted echo sounders. *J. Atmos. Oceanic Technol.*, **27**, 507–527, <https://doi.org/10.1175/2009JTECHO686.1>.
- Elipot, S., and L. M. Beal, 2015: Characteristics, energetics, and origins of Agulhas current meanders and their limited influence on ring shedding. *J. Phys. Oceanogr.*, **45**, 2294–2314, <https://doi.org/10.1175/JPO-D-14-0254.1>.
- Emery, W. J., and R. E. Thomson, 2014: *Data Analysis Methods in Physical Oceanography*. 3rd ed. Elsevier Science, 728 pp.
- Garzoli, S. L., and A. L. Gordon, 1996: Origins and variability of the Benguela current. *J. Geophys. Res.*, **101**, 897–906, <https://doi.org/10.1029/95JC03221>.
- Gordon, A. L., 1985: Indian-Atlantic transfer of thermocline water at the Agulhas retroflection. *Science*, **227**, 1030–1033, <https://doi.org/10.1126/science.227.4690.1030>.
- Goschen, W. S., E. H. Schumann, K. S. Bernard, S. E. Bailey, and S. H. Deyzel, 2012: Upwelling and ocean structures off Algoa Bay and the South-East coast of South Africa. *Afr. J. Mar. Sci.*, **34**, 525–536, <https://doi.org/10.2989/1814232X.2012.749810>.
- , T. G. Bornman, S. H. Deyzel, and E. H. Schumann, 2015: Coastal upwelling on the far eastern Agulhas Bank associated with large meanders in the Agulhas current. *Cont. Shelf Res.*, **101**, 34–46, <https://doi.org/10.1016/j.csr.2015.04.004>.
- Hermes, J., I. Ansoorge, L. Beal, S. Elipot, D. Byrne, and H. Ridderinkhof, 2020: Processed and corrected CTD profile data from ASCA July 2016 (SEAmester I), collected on the SA Agulhas II voyage 020. South African Environmental Observation Network (SAEON), accessed June 2020, <https://doi.org/10.15493/SAEON.EGAGASINI.24000008>.
- Hernández-Guerra, A., and L. D. Talley, 2016: Meridional overturning transports at 30°S in the Indian and Pacific Oceans in 2002–2003 and 2009. *Prog. Oceanogr.*, **146**, 89–120, <https://doi.org/10.1016/j.pocean.2016.06.005>.
- Hutchings, L., 1994: The Agulhas bank: A synthesis of available information and a brief comparison with other east-coast shelf regions. *S. Afr. J. Sci.*, **90**, 179–185.
- , L. E. Beckley, M. H. Griffiths, M. J. Roberts, S. Sundby, and C. Van der Lingen, 2002: Spawning on the edge: Spawning grounds and nursery areas around the southern African coastline. *Mar. Freshwater Res.*, **53**, 307–318, <https://doi.org/10.1071/MF01147>.
- Jackett, D. R., and T. J. McDougall, 1997: A neutral density variable for the world's oceans. *J. Phys. Oceanogr.*, **27**, 237–263, [https://doi.org/10.1175/1520-0485\(1997\)027<0237:ANDVFT>2.0.CO;2](https://doi.org/10.1175/1520-0485(1997)027<0237:ANDVFT>2.0.CO;2).
- Johns, W. E., T. Kanzow, and R. Zantopp, 2005: Estimating ocean transports with dynamic height moorings: An application in the Atlantic Deep Western Boundary Current at 26°N. *Deep-Sea Res. I*, **52**, 1542–1567, <https://doi.org/10.1016/j.dsr.2005.02.002>.
- Kanzow, T., U. Send, W. Zenk, A. D. Chave, and M. Rhein, 2006: Monitoring the integrated deep meridional flow in the tropical North Atlantic: Long-term performance of a geostrophic array. *Deep-Sea Res. I*, **53**, 528–546, <https://doi.org/10.1016/j.dsr.2005.12.007>.
- , and Coauthors, 2010: Seasonal variability of the Atlantic meridional overturning circulation at 26.5°N. *J. Climate*, **23**, 5678–5698, <https://doi.org/10.1175/2010JCLI3389.1>.
- Kerr, Y. H., P. Waldteufel, J. P. Wigneron, J. M. Martinuzzi, J. Font, and M. Berger, 2001: Soil moisture retrieval from space: The Soil Moisture and Ocean Salinity (SMOS) mission. *IEEE Trans. Geosci. Remote Sens.*, **39**, 1729–1735, <https://doi.org/10.1109/36.942551>.
- Laurindo, L. C., A. J. Mariano, and R. Lumpkin, 2017: An improved near-surface velocity climatology for the global ocean from drifter observations. *Deep-Sea Res. I*, **124**, 73–92, <https://doi.org/10.1016/j.dsr.2017.04.009>.
- Leber, G. M., and L. M. Beal, 2014: Evidence that Agulhas Current transport is maintained during a meander. *J. Geophys. Res. Oceans*, **119**, 3806–3817, <https://doi.org/10.1002/2014JC009802>.
- , and —, 2015: Local water mass modifications by a solitary meander in the Agulhas Current. *J. Geophys. Res. Oceans*, **120**, 4501–4515, <https://doi.org/10.1002/2015JC010863>.
- , —, and S. Elipot, 2017: Wind and current forcing combine to drive strong upwelling in the Agulhas Current.

- J. Phys. Oceanogr.*, **47**, 123–134, <https://doi.org/10.1175/JPO-D-16-0079.1>.
- Malan, N., B. Backeberg, A. Biastoch, J. V. Durgadoo, A. Samuelsen, C. Reason, and J. Hermes, 2018: Agulhas current meanders facilitate shelf-slope exchange on the eastern Agulhas bank. *J. Geophys. Res. Oceans*, **123**, 4762–4778, <https://doi.org/10.1029/2017JC013602>.
- Marsh, R., W. Hazeleger, A. Yool, and E. J. Rohling, 2007: Stability of the thermohaline circulation under millennial CO<sub>2</sub> forcing and two alternative controls on Atlantic salinity. *Geophys. Res. Lett.*, **34**, L03605, <https://doi.org/10.1029/2006GL027815>.
- Martin, M., and Coauthors, 2012: Group for High Resolution Sea Surface temperature (GHRSSST) analysis fields inter-comparisons. Part 1: A GHRSSST multi-product ensemble (GMPE). *Deep-Sea Res. II*, **77–80**, 21–30, <https://doi.org/10.1016/j.dsr2.2012.04.013>.
- McCarthy, G. D., and Coauthors, 2015: Measuring the Atlantic Meridional Overturning Circulation at 26°N. *Prog. Oceanogr.*, **130**, 91–111, <https://doi.org/10.1016/j.pocean.2014.10.006>.
- McDonagh, E. L., K. J. Heywood, and M. P. Meredith, 1999: On the structure, paths, and fluxes associated with Agulhas rings. *J. Geophys. Res.*, **104**, 21 007–21 020, <https://doi.org/10.1029/1998JC900131>.
- , and Coauthors, 2015: Continuous estimate of Atlantic oceanic freshwater flux at 26.5°N. *J. Climate*, **28**, 8888–8906, <https://doi.org/10.1175/JCLI-D-14-00519.1>.
- McMonigal, K., L. M. Beal, S. Elipot, K. L. Gunn, J. Hermes, T. Morris, and A. Houk, 2020: The impact of meanders, deepening and broadening, and seasonality on Agulhas Current temperature variability. *J. Phys. Oceanogr.*, **50**, 3529–3544, <https://doi.org/10.1175/JPO-D-20-0018.1>.
- Meinen, C. S., and D. R. Watts, 2000: Vertical structure and transport on a transect across the North Atlantic Current near 42°N: Time series and mean. *J. Geophys. Res.*, **105**, 21 869–21 891, <https://doi.org/10.1029/2000JC900097>.
- Morris, T., and Coauthors, 2017: The importance of monitoring the Greater Agulhas Current and its inter-ocean exchanges using large mooring arrays. *S. Afr. J. Sci.*, **113**, 1–7, <https://doi.org/10.17159/SAJS.2017/20160330>.
- Porri, F., J. M. Jackson, C. E. Von der Meden, N. Weidberg, and C. D. McQuaid, 2014: The effect of mesoscale oceanographic features on the distribution of mussel larvae along the south coast of South Africa. *J. Mar. Syst.*, **132**, 162–173, <https://doi.org/10.1016/j.jmarsys.2014.02.001>.
- Qiu, B., 2001: Kuroshio and Oyashio currents. *Encyclopedia of Ocean Sciences*, 2nd ed. J. H. Steele, Eds., Academic Press, 358–369, <https://doi.org/10.1016/B978-012374473-9.00350-7>.
- Reason, C. J., J. R. Lutjeharms, J. Hermes, A. Biastoch, and R. E. Roman, 2003: Inter-ocean fluxes south of Africa in an eddy-permitting model. *Deep-Sea Res. II*, **50**, 281–298, [https://doi.org/10.1016/S0967-0645\(02\)00385-5](https://doi.org/10.1016/S0967-0645(02)00385-5).
- Richardson, P. L., 2007: Agulhas leakage into the Atlantic estimated with subsurface floats and surface drifters. *Deep-Sea Res. I*, **54**, 1361–1389, <https://doi.org/10.1016/j.dsr.2007.04.010>.
- Rodríguez-Santana, A., J. L. Pelegrí, P. Sangrà, and A. Marrero-Díaz, 1999: Diapycnal mixing in Gulf Stream meanders. *J. Geophys. Res.*, **104**, 25 891–25 912, <https://doi.org/10.1029/1999JC900219>.
- Rouault, M., P. Penven, and B. Pohl, 2009: Warming in the Agulhas Current system since the 1980's. *Geophys. Res. Lett.*, **36**, L12602, <https://doi.org/10.1029/2009GL0137987>.
- Russo, C., T. Lamont, G. Tutt, M. van den Berg, and R. Barlow, 2019: Hydrography of a shelf ecosystem inshore of a major Western Boundary Current. *Estuarine Coastal Shelf Sci.*, **228**, 106363, <https://doi.org/10.1016/j.ecss.2019.106363>.
- Schauer, U., and M. Losch, 2019: “Freshwater” in the Ocean is not a useful parameter in climate research. *J. Phys. Oceanogr.*, **49**, 2309–2321, <https://doi.org/10.1175/JPO-D-19-0102.1>.
- Simon, M. H., K. L. Arthur, I. R. Hall, F. J. Peeters, B. R. Loveday, S. Barker, M. Ziegler, and R. Zahn, 2013: Millennial-scale Agulhas Current variability and its implications for salt-leakage through the Indian-Atlantic Ocean Gateway. *Earth Planet. Sci. Lett.*, **383**, 101–112, <https://doi.org/10.1016/j.epsl.2013.09.035>.
- Sloyan, B. M., K. R. Ridgway, and R. Cowley, 2016: The East Australian current and property transport at 27°S from 2012 to 2013. *J. Phys. Oceanogr.*, **46**, 993–1008, <https://doi.org/10.1175/JPO-D-15-0052.1>.
- Sprintall, J., S. E. Wijffels, R. Molcard, and I. Jaya, 2009: Direct estimates of the Indonesian throughflow entering the Indian Ocean: 2004–2006. *J. Geophys. Res. Oceans*, **114**, C07001, <https://doi.org/10.1029/2008JC005257>.
- Stramma, L., 1989: The Brazil current transport south of 23°S. *Deep-Sea Res.*, **36A**, 639–646, [https://doi.org/10.1016/0198-0149\(89\)90012-5](https://doi.org/10.1016/0198-0149(89)90012-5).
- van Ballegooyen, R. C., M. L. Grundlingh, and J. R. Lutjeharms, 1994: Eddy fluxes of heat and salt from the southwest Indian Ocean into the southeast Atlantic Ocean: A case study. *J. Geophys. Res.*, **99**, 14 053–14 070, <https://doi.org/10.1029/94JC00383>.
- Watts, D. R., and H. T. Rossby, 1977: Measuring dynamic heights with inverted echo sounders: Results from MODE. *J. Phys. Oceanogr.*, **7**, 345–358, [https://doi.org/10.1175/1520-0485\(1977\)007<0345:MDHWIE>2.0.CO;2](https://doi.org/10.1175/1520-0485(1977)007<0345:MDHWIE>2.0.CO;2).
- , C. Sun, and S. Rintoul, 2001: A two-dimensional gravest empirical mode determined from hydrographic observations in the Subantarctic Front. *J. Phys. Oceanogr.*, **31**, 2186–2209, [https://doi.org/10.1175/1520-0485\(2001\)031<2186:ATDGEM>2.0.CO;2](https://doi.org/10.1175/1520-0485(2001)031<2186:ATDGEM>2.0.CO;2).
- Weijer, W., W. P. De Ruijter, H. A. Dijkstra, and P. J. Van Leeuwen, 1999: Impact of interbasin exchange on the Atlantic overturning circulation. *J. Phys. Oceanogr.*, **29**, 2266–2284, [https://doi.org/10.1175/1520-0485\(1999\)029<2266:IOIEOT>2.0.CO;2](https://doi.org/10.1175/1520-0485(1999)029<2266:IOIEOT>2.0.CO;2).
- , and Coauthors, 2019: Stability of the Atlantic Meridional Overturning Circulation: A review and synthesis. *J. Geophys. Res. Oceans*, **124**, 5336–5375, <https://doi.org/10.1029/2019JC015083>.
- Wijffels, S. E., G. Meyers, and S. J. Godfrey, 2008: A 20-yr average of the Indonesian throughflow: Regional currents and the interbasin exchange. *J. Phys. Oceanogr.*, **38**, 1965–1978, <https://doi.org/10.1175/2008JPO3987.1>.